

ARTICLE

Open Access

# In situ XRD and operando spectra-electrochemical investigation of tetragonal $\text{WO}_{3-x}$ nanowire networks for electrochromic supercapacitors

Shen Wang<sup>1</sup>, Hongbo Xu<sup>1</sup>, Tingting Hao<sup>1</sup>, Peiyuan Wang<sup>2</sup>, Xiang Zhang<sup>3</sup>, Hongming Zhang<sup>1</sup>, Junying Xue<sup>1</sup>, Jiupeng Zhao<sup>1</sup> and Yao Li<sup>3</sup>

## Abstract

Electrochromic supercapacitors (ESCs) are appealing for smart electronic device applications due to their advantages of dual-function integration. Unfortunately, the synchronous dual-function evaluation and the essential reaction mechanism are ambiguous. Herein, we constructed a 3D  $\text{WO}_{3-x}$  nanowire networks/fluorine-doped tin oxide ( $\text{WO}_{3-x}$  NWNs/FTO) bifunctional electrode for ESCs by a solvothermal self-crystal seeding method. The synchronous correspondence relationship between the optical and electrochemical performances of the  $\text{WO}_{3-x}$  NWNs/FTO electrode was explored using an operando spectra-electrochemical characterization method. It reveals an excellent areal capacity of  $57.57 \text{ mF cm}^{-2}$  with a high corresponding optical modulation ( $\Delta T$ ) of 85.05% and high optical-electrochemical cycling stability. Furthermore, the synergistic reaction mechanism between the  $\text{Al}^{3+}$  ion intercalation behavior and the surface pseudocapacitance reaction during electrochemical cycling is revealed utilizing in situ X-ray diffraction. Based on these results, an ESC device was constructed by pairing  $\text{WO}_{3-x}$ /FTO as the cathode with  $\text{V}_2\text{O}_5$  nanoflowers/FTO ( $\text{V}_2\text{O}_5$  NFs/FTO) as the anode, which simultaneously deliver high capacity and large optical modulation. Moreover, the energy storage level of the ESC device could be visually monitored by rapid and reversible color transitions in real time. This work provides a promising pathway to developing multi-functional integrated smart supercapacitors.

## Introduction

As smart power systems, electrochromic supercapacitor (ESC) devices have attracted increasing attention. This is because they have the capability to monitor the energy storage level of the device in real time through color change, which makes the energy storage devices more advanced<sup>1</sup>.

Much effort has been devoted to promoting the wide application of ESC devices. In general, the energy storage

and electrochromic performance of ESC devices are mainly influenced by the performance of bifunctional electrodes. Hence, high-performance bifunctional electrodes need to be constructed<sup>2–6</sup>. For example, Kim et al.<sup>2</sup> presented  $\text{WO}_3$ -embedded Au nanofilament array bifunctional electrodes, which exhibited a specific capacity of  $202 \text{ F g}^{-1}$  at  $5 \text{ mV s}^{-1}$  ( $-0.9$  to  $0.45 \text{ V vs. Hg/Hg}_2\text{Cl}_2$ ) and a high  $\Delta T$  of 67.49% by applying potential steps of  $\pm 0.75 \text{ V}$  (vs.  $\text{Hg/Hg}_2\text{Cl}_2$ ). Shen et al.<sup>4</sup> prepared tungsten oxide/titanium dioxide nanorod arrays on an FTO substrate, which showed a  $\Delta T$  of 78% at pulse-type voltage ( $\pm 3 \text{ V vs. Ag/AgCl}$ ) and specific capacitance of  $426.8 \text{ F g}^{-1}$  at a current density of  $1 \text{ A g}^{-1}$  with a voltage window of  $-1.2$  to  $0 \text{ V vs. Ag/AgCl}$ . In addition, all ESC devices have also been developed<sup>3,4,7–12</sup>. For instance, Yun et al. fabricated an ESC device using an indium tin oxide

Correspondence: Jiupeng Zhao (jzhaohit@hit.edu.cn) or Yao Li (yaoli@hit.edu.cn)

<sup>1</sup>School of Chemistry and Chemical Engineering, Harbin Institute of Technology, 150001 Harbin, PR China

<sup>2</sup>Henan Provincial Key Laboratory of Surface and Interface Science, Department of Materials and Chemical Engineering, Zhengzhou University of Light Industry, 450002 Zhengzhou, PR China

Full list of author information is available at the end of the article

© The Author(s) 2021



**Open Access** This article is licensed under a Creative Commons Attribution 4.0 International License, which permits use, sharing, adaptation, distribution and reproduction in any medium or format, as long as you give appropriate credit to the original author(s) and the source, provide a link to the Creative Commons license, and indicate if changes were made. The images or other third party material in this article are included in the article's Creative Commons license, unless indicated otherwise in a credit line to the material. If material is not included in the article's Creative Commons license and your intended use is not permitted by statutory regulation or exceeds the permitted use, you will need to obtain permission directly from the copyright holder. To view a copy of this license, visit <http://creativecommons.org/licenses/by/4.0/>.

(ITO) glass electrode and  $\text{WO}_{3-x}$ /ITO glass electrode, which exhibited a large  $\Delta T$  ( $\sim 91\%$ ) with a pulse-type voltage (between  $-1.5$  and  $0$  V) and high areal capacitance ( $\sim 13.6 \text{ mF cm}^{-2}$ ) at  $0.4 \text{ mA cm}^{-2}$  within a potential range of  $-1.5$  to  $0$  V<sup>13</sup>. Subsequently, Guo et al.<sup>9</sup> constructed a solid-state ESC device with poly(5-formylindole)/ $\text{WO}_3$ /ITO and poly(3,4-ethylenedioxythiophene)/ITO. The device showed a  $\Delta T$  of  $55\%$  under square-wave potentials from  $0$  V to  $+1.0$  V with step times of  $5$  s and an areal specific capacitance of  $10.38 \text{ mF cm}^{-2}$  at a current density of  $0.025 \text{ mA cm}^{-2}$  under a voltage range of  $0.0$ – $1.0$  V.

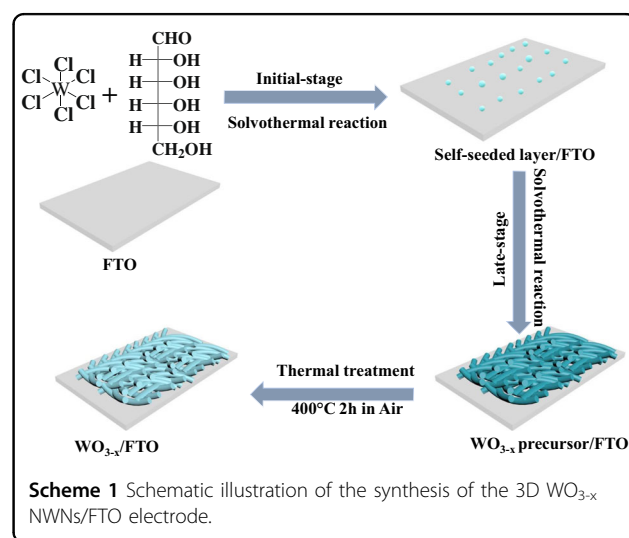
Despite the above achievements, to the best of our knowledge, the capacitance and optical modulation of the bifunctional electrodes or ESC devices reported in many papers have not been measured synchronously. In other words, the electrochromic performances were normally tested by stepping between a positive and negative voltage, while the energy storage performances were carried out under continuous voltage or current conditions. Thus, it is difficult to accurately determine the correspondence between the energy storage capacity and optical modulation due to their separated measurements<sup>7,8</sup>. Moreover, the crystal evolution and ion storage mechanism of the dual-functional electrode is ambiguous. This is because the structural evolution of the bifunctional electrode is not continuously monitored in the optical-electrochemical change process; thus, it is impossible to determine how ions embed or adsorb on the lattice or surface of the electrode material. However, the well-defined reaction mechanism is helpful for selecting the best counter electrode and electrolyte when constructing high-performance ESC devices and optimizing or designing electrode materials of this crystal type. To address these challenges, *in situ/operando* characterization techniques, including *in situ* X-ray diffraction and *operando* spectra-electrochemical characterizations, need to be introduced. These tools can provide valuable information on bifunctional electrodes in charge/discharge processes, such as the evolution of the crystalline structure and the relationship between energy storage capability and optical modulation.

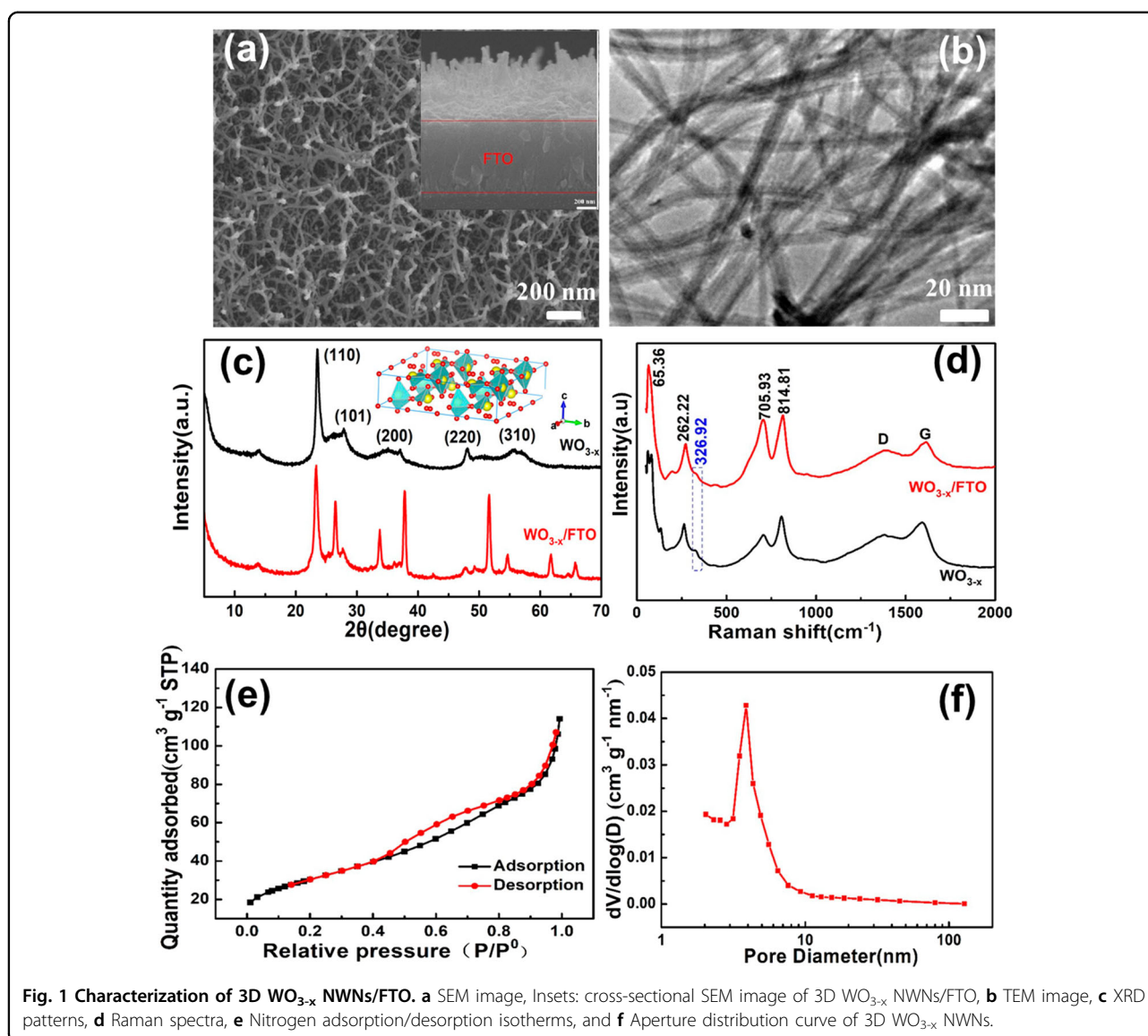
Herein,  $3\text{D WO}_{3-x}$  nanowire networks self-assembled on FTO by a solvothermal reaction and annealing treatment. This self-seeded growth strategy can significantly accelerate the charge transfer between the  $\text{WO}_{3-x}$  layer and FTO layer. To determine the corresponding relationship between the optical and electrochemical performances of the electrode, we employ *operando* spectra-electrochemical characterization techniques, which exhibit high areal capacities ( $57.57 \text{ mF cm}^{-2}$ ) with a corresponding  $\Delta T$  of  $85.05\%$  due to the material's unique  $3\text{D}$  crosslinked nanowire network and hierarchical pore structure. In addition, to probe the opto-electrochemical mechanism of the aluminum ions embedded into the

tetragonal  $\text{WO}_{3-x}$  electrode, *in situ* X-ray diffraction characterization techniques were employed, which revealed that the synergistic mechanism between the  $\text{Al}^{3+}$  ion intercalation behavior and the surface pseudocapacitance reaction occurred during the electrochemical process. As a proof of concept, a superior ESC device, which comprises a  $3\text{D WO}_{3-x}$  NWNs/FTO cathode and  $\text{V}_2\text{O}_5$  NFs/FTO anode, has been achieved. The  $\text{V}_2\text{O}_5$  NF/FTO electrode not only has a high transmittance but also matches well with the  $\text{WO}_{3-x}$  NWN electrode in terms of the capacity, reaction mechanism and voltage window. The device is equipped with a high capacity and homologous optical modulation. Specifically, the visualization of the energy storage level for the ESC is achieved by reversible color changes from dark blue to transparent during the electrochemical cycle process. Our work paves the way for the development of an intelligent transparent capacitor.

## Results and discussion

As shown in Scheme 1, the  $3\text{D WO}_{3-x}$  NWN/FTO dual-functional electrode was prepared by combining a solvothermal method and subsequent thermal treatment. At the beginning of the solvothermal reaction, glucose acted as a bridge to link the tungsten trioxide crystal nucleus with FTO. Under the influence of hydrogen bonding forces and other physical adsorption, the tungsten trioxide crystal seed layer spontaneously formed on the FTO. In the subsequent solvothermal process,  $\text{WO}_{3-x}$  precursor nanowires grew along the  $[110]$  direction of the seed layer of the FTO. Additionally, a crosslinking nanowire network of the  $\text{WO}_{3-x}$  precursor self-assembly progressively occurred on FTO to reduce the surface energy<sup>14</sup>. Then, the prepared  $\text{WO}_{3-x}$ /FTO was heat-treated at  $400^\circ\text{C}$  for  $2$  h, and thermal gravimetric analysis (TGA) was performed on the  $\text{WO}_{3-x}$  precursor in an air atmosphere





(Supplementary Fig. S1) to remove the excess carbon and impurities, eliminating the color effect of carbon and forming crystalline  $\text{WO}_{3-x}$ . As shown in a typical field emission scanning electron microscope (FESEM) image of the 3D  $\text{WO}_{3-x}$  NWNs/FTO (Fig. 1a), the interconnected  $\text{WO}_{3-x}$  nanowires are uniformly anchored on the FTO substrate, forming 3D disordered crosslinking networks with randomly distributed pores. This unique structure can provide numerous active sites and shorten the diffusion path of the ions and electrons. Additionally, it can alleviate the mechanical stress of ion insertion/extraction in the charging/discharging process. From the cross-sectional SEM image in the inset of Fig. 1a, the cross-linking  $\text{WO}_{3-x}$  nanowire networks with a thickness of  $730 \pm 20$  nm self-assembled on FTO.

Microcosmic information about the  $\text{WO}_{3-x}$  NWNs/FTO was obtained from transmission electron microscopy (TEM) and high-resolution TEM (HRTEM). Figure 1b and Supplementary Fig. S2 also confirm that the  $\text{WO}_{3-x}$  NWNs show a crosslinked nanowire network structure, and a single  $\text{WO}_{3-x}$  nanowire is  $\sim 4\text{--}10$  nm in diameter and  $\sim 1\text{--}2$   $\mu\text{m}$  in length. In addition, the HRTEM image shows the high crystallinity of the single nanowire, and the 0.36 nm lattice spacing corresponds to the (110) crystal plane of tetragonal  $\text{WO}_{3-x}$  (Supplementary Fig. S3).

The crystal structure of the prepared samples was investigated by XRD analysis, and the results are shown in Fig. 1c. For the  $\text{WO}_{3-x}$  powders, all the peaks in the XRD pattern are well matched with the tetragonal structure

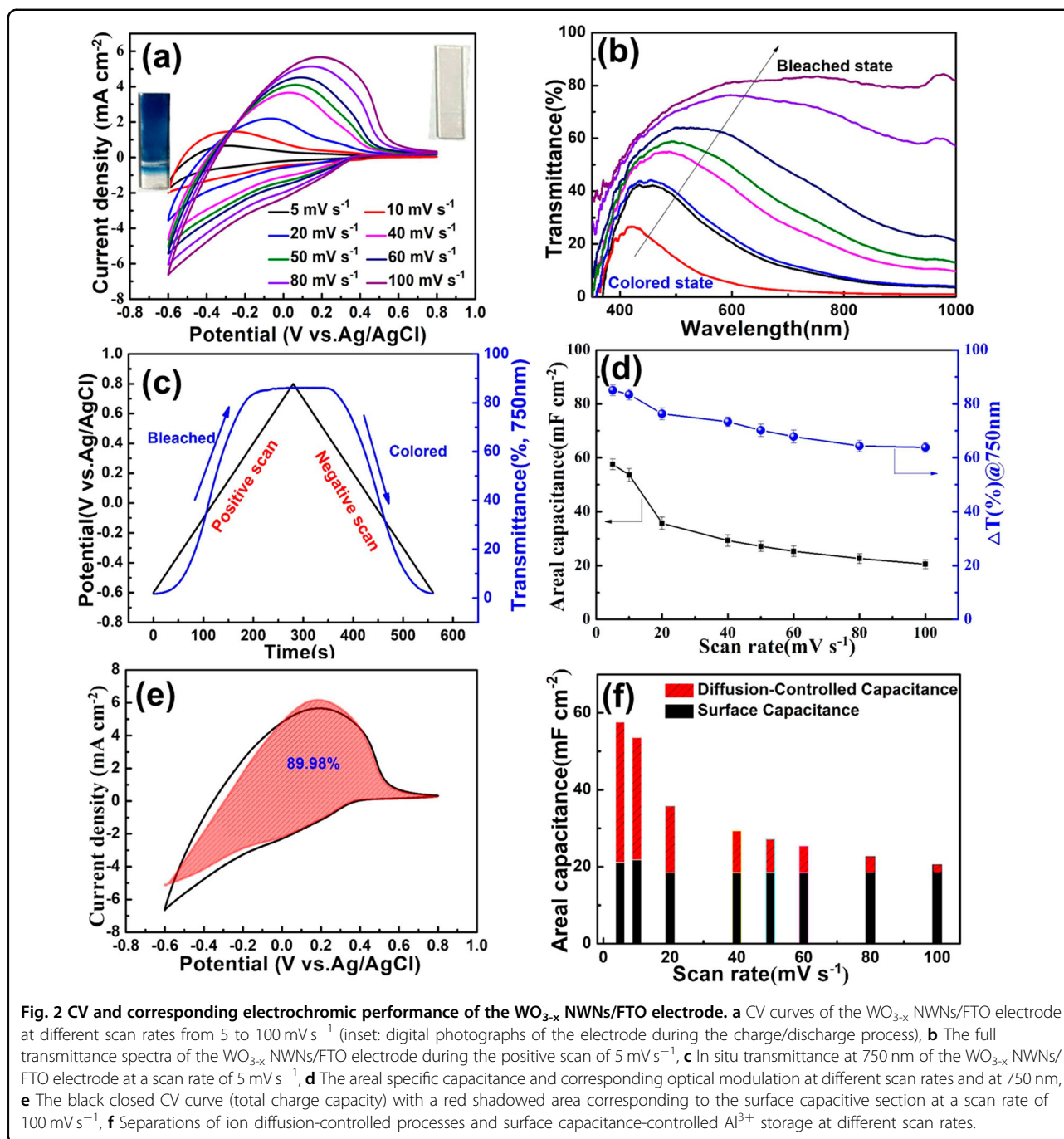
(P4/nmm) phase of nonstoichiometric  $\text{WO}_3$  (with lattice constants of  $a = b = 5.31 \text{ \AA}$ ,  $c = 3.93 \text{ \AA}$ , JCPDS card no. 89-8052), which confirms the successful preparation of  $\text{WO}_{3-x}$ . The obvious diffraction peaks at  $\sim 23.7^\circ$ ,  $27.8^\circ$ ,  $35.3^\circ$ ,  $48.1^\circ$ , and  $55.7^\circ$  correspond well to the (110), (101), (200), (220), and (310) crystal planes of  $\text{WO}_{3-x}$ , respectively, and no impurity peaks can be observed. Moreover, the peak intensity of the (110) crystal plane is significantly stronger, which indicates that  $\text{WO}_{3-x}$  nanowires are preferentially grown along the [110] crystal plane orientation<sup>15</sup>. This observation is in accordance with the results of HRTEM. The diffraction peaks of  $\text{WO}_{3-x}$  NWNs/FTO glass are consistent with those of the  $\text{WO}_{3-x}$  powders when several FTO diffraction peaks are deducted (JCPDS card no. 46-1088). To further evaluate the structure of the prepared samples, Raman spectroscopy was applied to reveal the various variations in crystalline symmetry and microstructure (Fig. 1d). In the Raman spectrum of  $\text{WO}_3$  NWN powders, two peaks at  $696.56$  and  $801.63 \text{ cm}^{-1}$  represent the stretching modes of  $\text{O}-\text{W}^{6+}-\text{O}$ . The peak at  $258.12 \text{ cm}^{-1}$  is attributed to the bending vibration mode of the bridging oxygen, while the peak at  $59.31 \text{ cm}^{-1}$  arises due to the vibration of the lattice<sup>16,17</sup>. A broadened Raman peak at  $\sim 989.11 \text{ cm}^{-1}$  belonging to the terminal  $\text{W}=\text{O}$  bond on the surface is observed. The integrated intensity ratio of  $\text{W}=\text{O}/\text{O}-\text{W}^{6+}-\text{O}$  for  $\text{WO}_{3-x}$  NWNs is 0.53, indicating its high crystallinity<sup>18</sup>. Moreover, two absorption bands at  $1374.64$  and  $1596.88 \text{ cm}^{-1}$  belong to the D and G bands of carbon, respectively, where the carbon is derived primarily from the carbonation of glucose. The presence of a small amount of carbon is expected to increase the conductivity of  $\text{WO}_{3-x}$  without affecting the transparency of the electrode. In addition, a weak Raman peak at  $327.75 \text{ cm}^{-1}$  belongs to the bending mode  $\text{O}-\text{W}^{5+}-\text{O}$ <sup>16,17</sup>. In the spectrum of the  $\text{WO}_{3-x}$  NWNs/FTO, similar Raman vibrations could be observed at  $65.36$ ,  $262.22$ ,  $705.93$ , and  $814.81 \text{ cm}^{-1}$ , along with two additional features at  $1386.73$  and  $1614.43 \text{ cm}^{-1}$  that were due to the remaining carbon. The estimated intensity ratio of  $\text{W}=\text{O}/\text{O}-\text{W}^{6+}-\text{O}$  for 3D  $\text{WO}_{3-x}$  NWNs/FTO is 0.68, also revealing the high crystallinity of  $\text{WO}_{3-x}$  nanowires. Moreover, a weak Raman peak at  $326.92 \text{ cm}^{-1}$  is attributed to the bending mode  $\text{O}-\text{W}^{5+}-\text{O}$ , affirming the presence of a small amount of  $\text{W}^{5+}$  in  $\text{WO}_{3-x}$  NWNs/FTO. These results strongly suggest the successful preparation of tetragonal  $\text{WO}_{3-x}$  NWNs on FTO glass.

To evaluate the constitutive properties of the  $\text{WO}_{3-x}$  NWNs in depth, Brunauer-Emmett-Teller (BET) measurements were carried out. As seen from Fig. 1(e and f), the isotherm of  $\text{WO}_{3-x}$  NWNs reveals a distinct hysteresis loop in the relative pressure ( $P/P_0$ ) range of 0.4–0.85, which is attributed to a typical Langmuir type IV adsorption isotherm. This isotherm clearly illustrates that the  $\text{WO}_{3-x}$  NWNs possess a mesoporous structure. The

pore size distribution of the  $\text{WO}_{3-x}$  NWNs according to the Barrett-Joyner-Halenda (BJH) analysis is within a very narrow range of 3–5 nm, which is derived from the nanowire network structure of tungsten trioxide. Nano-hierarchical porous frameworks are formed through integration with the macroporous structure that is shaped by the crosslinking nanowire networks. These networks are propitious to the diffusion of ions, improving the dynamic behaviors of the electrode, achieving rapid redox energy storage and color transformation, and easing volume expansion. According to the multipoint BET formula, the specific surface area of  $\text{WO}_{3-x}$  NWNs is  $109.8 \text{ m}^2\text{-g}^{-1}$ , which is superior to that of many other  $\text{WO}_3$ -based materials<sup>19–22</sup>. The higher specific surface area of the 3D  $\text{WO}_{3-x}$  NWNs/FTO electrode allows for enough electroactive sites for the electrochemical reaction to occur, improving the energy storage and the corresponding optical performance.

X-ray photoelectron spectroscopy (XPS) was used to analyze the elemental composition and valence state of  $\text{WO}_{3-x}$  NWNs/FTO. The offset of the binding energy of the spectrum was calibrated with the C 1s peak ( $284.8 \text{ eV}$ ) as a reference. The full survey spectrum (Supplementary Fig. S4a) indicates the coexistence of W, O, C, F, and Sn, among which Sn and F originate from the FTO substrate<sup>23</sup>. In the W 4f spectrum (Supplementary Fig. S4b), the binding energy peaks at  $35.88$  and  $38.08 \text{ eV}$  are indexed to  $\text{W}^{6+}$ , and those at  $34.78$  and  $36.88 \text{ eV}$  originate from  $\text{W}^{5+}$ <sup>16,17</sup>. The relative percentages of  $\text{W}^{6+}$  and  $\text{W}^{5+}$  in the  $\text{WO}_{3-x}$  NWNs on FTO are calculated to be  $\sim 92.07\%$  and  $7.93\%$ , respectively. Hence, the O/W atomic ratio is  $\sim 2.92$ , indicating that the  $\text{WO}_{3-x}$  NWNs are multivalent and nonstoichiometric; this result is aligned with the XRD results. In addition, the binding energy peak at  $41.61 \text{ eV}$  belongs to the W  $5p_{3/2}$  level, which confirms the growth of  $\text{WO}_{3-x}$  NWNs. As shown in Supplementary Fig. S4c, the O 1s binding energy peak can be resolved into three components at  $\sim 530.7$ ,  $531.3$ , and  $532.8 \text{ eV}$ , belonging to  $\text{W}-\text{O}$  bonds derived from  $\text{WO}_{3-x}$ ,  $\text{W}-\text{O}-\text{C}$  bonds, and  $-\text{OH}$  and/or  $\text{C}-\text{O}-\text{C}$  bonds stemming from the doped carbon and absorbed  $\text{H}_2\text{O}$ , respectively<sup>24</sup>. Therefore, the  $\text{W}-\text{O}-\text{C}$  bond reveals that the covalent bond between the  $\text{WO}_3$  nanowires and glucose is built, which can increase the conductivity of  $\text{WO}_3$ , resulting in rapid electron transport and an excellent rate performance. The XPS results further confirm that  $\text{WO}_3$  NWNs grow directly on the FTO substrate.

To monitor the charge storage state of the  $\text{WO}_{3-x}$  NWNs/FTO electrode by color, we employed the operando spectra-electrochemical characterization method. The synchronous operando test could show the correlation between the quantity of stored charge and the optical property of the charging/discharging process. Hence, cyclic voltammetry (CV) curves and optical profiles of the



$\text{WO}_{3-x}$  NWNs/FTO electrode are obtained synchronously at different scan rates, and the results are shown in Fig. 2(a, b, and c), Supplementary Fig. S5 and Fig. S6. All CV curves (Fig. 2a) show the nonrectangular form, which indicates the typical pseudocapacitive behavior of the reversible redox reaction. With increasing scan rate, the shape of the curves is almost unchanged compared with those at low scan rates, indicating good dynamic reversibility of the  $\text{WO}_{3-x}$  NWNs/FTO electrode. In Fig. 2b, each point along

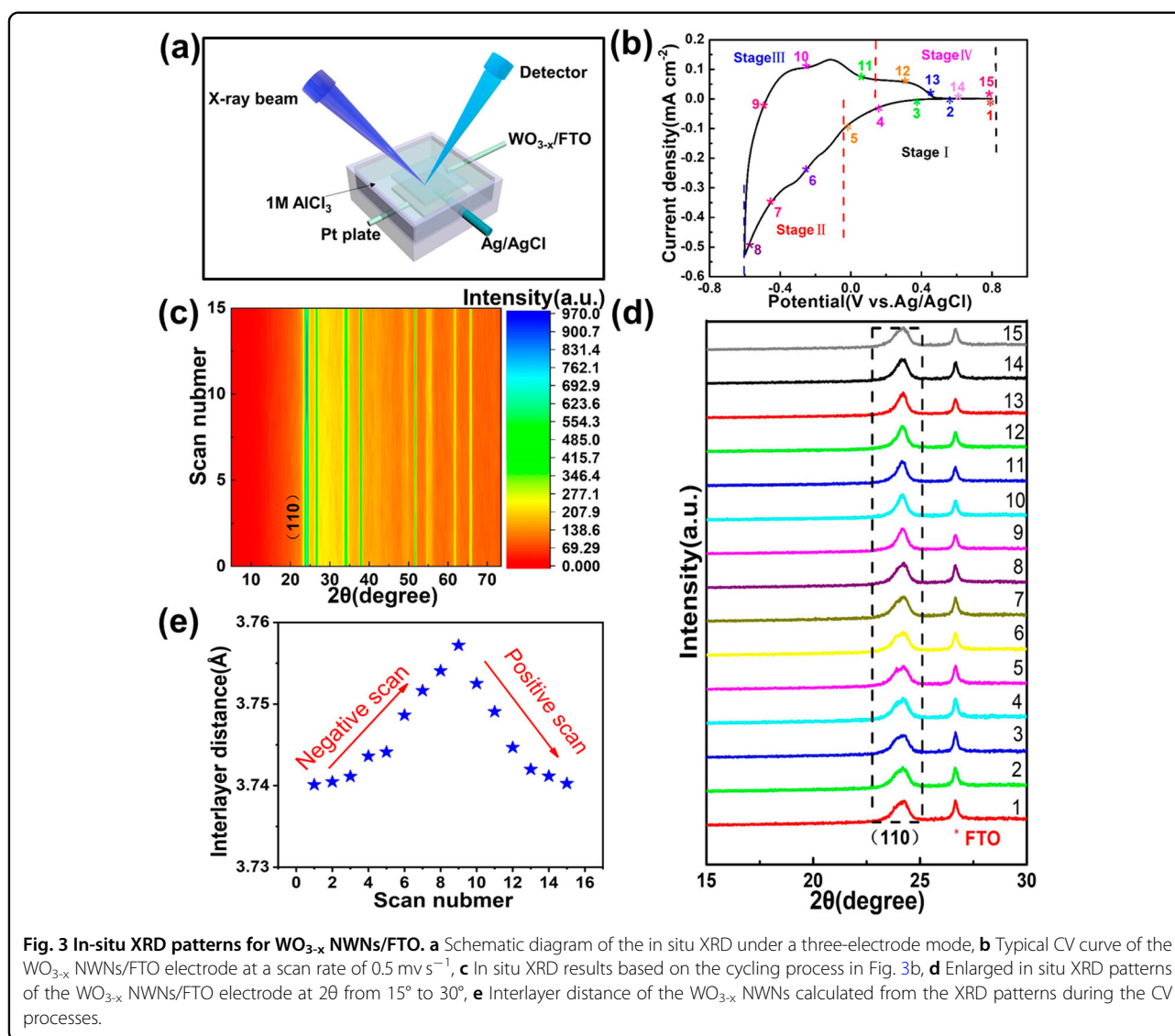
the CV curve has a corresponding full transmittance curve, which shows that the electrode simultaneously exhibits the phenomena of energy storage and discoloration on the macro level during the microscopic electrochemical reaction. It is further confirmed that the energy storage and discoloration are synchronous; that is, the energy storage state can be monitored by color visualization. In Fig. 2c and Fig. S5a, the  $\Delta T$  of the  $\text{WO}_{3-x}$  NWNs/FTO electrode is  $\sim 85.05\%$  at 750 nm and  $\sim 70.68\%$  at 550 nm at a voltage

of 0.8 V, respectively, and the electrode becomes colorless and transparent due to double extraction of aluminum ions and electrons. During the negative scan, the transmittance of the electrode gradually decreases, and the color of the electrode gradually turns dark blue. In addition, this result also confirms that the transmittance of the electrode is different and can be controlled by voltage in the visible or near infrared ranges of light. As seen in Supplementary Figs. S5, S6, and S7 and Table S1, under the same scanning speed, the  $\Delta T$  of the electrode is different at different wavelengths, but the change trend is consistent. At different scanning speeds, the time required to reach the same  $\Delta T$  at the same wavelength is different. This observation is consistent with the change in the CV curve under different scanning speeds, further proving that it is feasible to monitor the energy storage level by color. Additionally, it can be found that the modulation ability of the electrode in the visible light region is better than that in the near infrared light region at high scanning speed. The areal capacitance and corresponding optical modulation of the  $\text{WO}_{3-x}$  NWNs/FTO electrode based on the discharging processes of different scan rates were calculated according to Supplementary Equation 1, and the results are shown in Fig. 2d. The  $\text{WO}_{3-x}$  NWNs/FTO electrode shows a specific capacitance of  $57.57 \text{ mF cm}^{-2}$  and a corresponding  $\Delta T$  of 85.05% at 750 nm at a scan rate of  $5 \text{ mV s}^{-1}$ . Even when the sweep speed increases to  $100 \text{ mV s}^{-1}$ , the electrodes can still display a specific capacitance of  $20.53 \text{ mF cm}^{-2}$  and a corresponding  $\Delta T$  of 62.34% at 750 nm. These results indicate that the  $\text{WO}_{3-x}$  NWNs/FTO electrode can maintain a high optical-electrochemical performance throughout the electrochemical process due to the crosslinked nanowire network structure of  $\text{WO}_{3-x}$ , ensuring the fast and effective delivery of  $\text{Al}^{3+}$  ions.

Moreover, CV curves also offer wider insight into the difference in charge storage kinetics. The capacitive effect and the diffusion-controlled process can be characterized by CV data analysis according to  $i = a\nu^b$ <sup>25</sup>. In the formula,  $I$  and  $\nu$  represent the current and scan rate, respectively, and  $a$  and  $b$  are adjustable parameters. When the  $b$  value approaches 0.5, the charge storage process is controlled by diffusion, and when the  $b$  value equals 1.0, a surface capacitive electrochemical reaction occurs. To calculate the  $b$  value of the  $\text{WO}_{3-x}$  NWNs/FTO electrode, the linear correlation between  $\log(i)$  and  $\log(\nu)$  at different potentials was fitted in Supplementary Fig. S8. The  $b$ -values for the  $\text{WO}_{3-x}$  NWNs/FTO electrode at different potentials are shown in Supplementary Fig. S9 and are 0.46, 0.68, 0.98, and 0.9. The synergistic reactions controlled by diffusion and surface redox are involved with the  $\text{Al}^{3+}$  ion storage behavior; these reactions affect the capacitance and optical modulation of the electrodes. Furthermore, the ratio of the surface capacity ( $k_1\nu$ ) to diffusion-

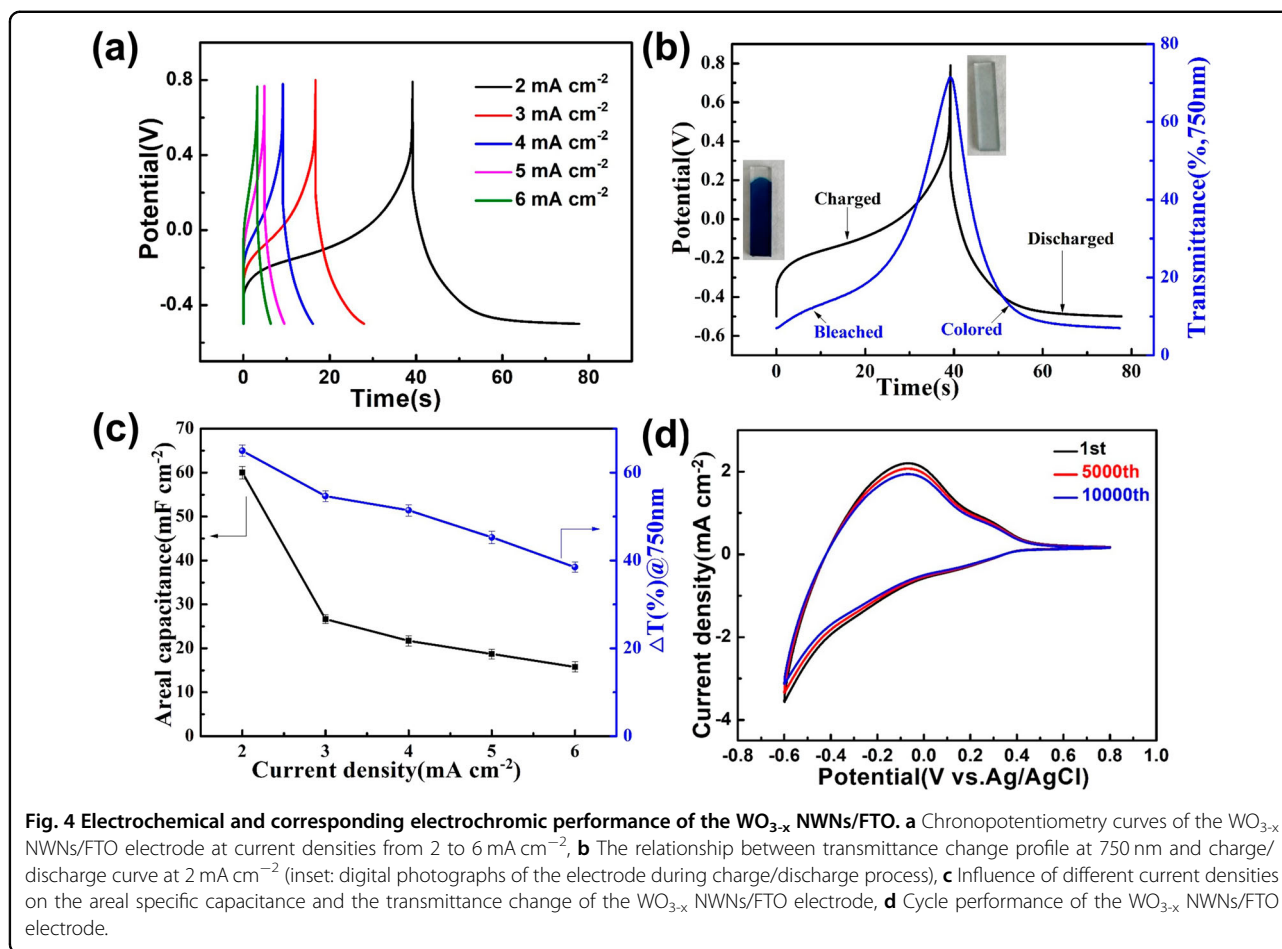
controlled intercalation ( $k_2\nu^{0.5}$ ) in the total capacity can be calculated based on the following equation:  $i = k_1\nu + k_2\nu^{0.5}$ <sup>26</sup>. Fig. 2e displays a high capacitance contribution of 89.98% at a scan rate of  $100 \text{ mV s}^{-1}$ . Generally, the surface process capacity can be divided into electrical-double-layer capacitance and surface redox capacitance, in which the electrical-double-layer type needs an ultrahigh specific surface area (such as carbon material of over  $2000 \text{ m}^2 \text{ g}^{-1}$ ) because its specific capacitance is mainly affected by the specific surface area<sup>27</sup>. Since the specific surface area of the  $\text{WO}_{3-x}$  NWNs/FTO electrode is  $109.8 \text{ m}^2 \cdot \text{g}^{-1}$ , the surface capacitance of the electrode is mainly attributed to the pseudocapacitive reaction. Moreover, the capacitance contributions for the total  $\text{Al}^{3+}$  storage capacity at different scan rates could be calculated, and the results are presented in Fig. 2f. It is obvious that with increasing scan rate, the contribution from diffusion-controlled capacitance gradually decreases; this trend indicates that a long relaxation time impedes  $\text{Al}^{3+}$  intercalation at higher scan rates. The surface reaction contribution capacitance remains stable owing to the good conductivity, high specific area, and crosslinking porous structure of the electrode. The 3D nanowire structure can supply abundant electrochemical active sites on the surface of  $\text{WO}_{3-x}$  to promote the adsorption of  $\text{Al}^{3+}$ , accelerate the surface redox reactions, and reinforce the energy collection efficiency<sup>28</sup>. Hence, we can affirm that the synergistic effects between the surface pseudocapacitance reaction and  $\text{Al}^{3+}$  intercalation reaction play a crucial role in the energy storage and electrochromic behaviors of the  $\text{WO}_{3-x}$  NWNs/FTO electrode.

To further probe the reaction mechanism of energy storage and the corresponding optical behaviors of the  $\text{WO}_{3-x}$  NWN/FTO electrode caused by  $\text{Al}^{3+}$  ions, we studied the crystal structure evolution of the  $\text{WO}_{3-x}$  NWN/FTO electrode during the actual electrochemical process using in situ XRD measurements. A schematic diagram of the in situ XRD measurement using a three-electrode polytetrafluoroethylene (PTFE) electrochemical cell is shown in Fig. 3a. The CV experiment and the corresponding structural evolution of the electrode were monitored synchronously at a scan rate of  $0.5 \text{ mV s}^{-1}$ , and the results are shown in Fig. 3b–d and Supplementary Fig. S10. In the full-scale in situ XRD patterns of the  $\text{WO}_{3-x}$  NWNs/FTO electrode, no other peaks are observed, except for the FTO and (110) of  $\text{WO}_{3-x}$  NWN peaks, revealing that no other phases are formed during the electrochemical cycling process. In stage I (0.8–0.0 V), the  $\text{WO}_{3-x}$  NWNs/FTO electrode starts to discharge, and the transmittance of the electrode decreases gradually. From the in situ XRD patterns, the  $2\theta$  degree and the peak intensity of the (110) crystal plane of  $\text{WO}_{3-x}$  NWNs remain unchanged, which indicates that the charge storage and optical modulation of the electrode are mainly



ascribed to the pseudocapacitive reaction due to the large surface area and nanohierarchical pore structure of  $\text{WO}_{3-x}$  NWNs<sup>29,30</sup>. In stage II (0.0 to  $-0.6 \text{ V}$ ), the color of the  $\text{WO}_{3-x}$  NWNs/FTO electrode transforms to dark blue with increasing electrode discharge depth. In terms of the microstructure, the (110) peak gradually shifts toward the lower  $2\theta$  degree ( $23.61^\circ$ ), which indicates that the lattice expands along the [110] direction, suggesting the insertion of  $\text{Al}^{3+}$  ions<sup>31,32</sup>. The increased interlayer distance can be attributed to the incremental interlayer electrostatic repulsion caused by the intercalation of aluminum ions. Moreover, the intensity of the peak decreases, revealing the conversion of  $\text{WO}_{3-x}$  NWNs into an amorphous phase during the discharge process. In the stage III ( $-0.6$  to  $0.15 \text{ V}$ ), the transmittance of the  $\text{WO}_{3-x}$  NWNs/FTO electrode gradually increases as electrode charging proceeds. Additionally, we found that the (110) peak located

at  $23.61^\circ$  gradually shifts toward  $23.77^\circ$  and that the interlayer space gradually decreases, demonstrating the extraction of the  $\text{Al}^{3+}$  ions. When the voltage is fully recharged back to  $0.8 \text{ V}$  (in stage IV), the tungsten trioxide electrode becomes transparent. From the in situ XRD pattern, the  $2\theta$  and intensity of the (110) peak of  $\text{WO}_{3-x}$  NWNs are restored to the original state. The interlayer distance ( $d_{110}$ ) values at the charging/discharging process were calculated and are shown in Fig. 3(e), which shows that the interlayered lattice variation of  $d_{110}$  is highly reversible. The largest expansion of  $d_{110}$  is  $\sim 0.02 \text{ \AA}$ , indicating that the lattice change of the  $\text{WO}_{3-x}$  NWNs can be considered negligible during the  $\text{Al}^{3+}$  ion insertion/extraction process, implying high cycling durability. Based on the electrochemical testing results, in situ XRD analysis and Supplementary Fig. S11, the mechanism of the charge storage and electrochromic behavior of the



$WO_{3-x}$  NWNs/FTO electrode can be attributed to the combined effect of the surface pseudocapacitive reaction and insertion/extraction process, which may be described as follows:

$Al^{3+}$  adsorption : surface pseudo capacitance (1)

$Al^{3+}$  intercalation :  $WO_{3-x} + yAl^{3+} + 3ye^{-} \rightarrow Al_yWO_{3-x}$  (2)

$Al^{3+}$  extraction :  $Al_yWO_{3-x} \rightarrow WO_{3-x} + yAl^{3+} + 3ye^{-}$  (3)

$Al^{3+}$  desorption : surface pseudo capacitance (4)

Benefitting from the surface pseudocapacitive and insertion/extraction behaviors, the  $WO_{3-x}$  NWNs/FTO electrode can display excellent charge storage and electrochromic performances. To further verify this result, chronopotentiometry (CP) and in situ spectroscopy measurements were conducted at different current densities. Furthermore, the feasibility of monitoring the charge storage level of the  $WO_{3-x}$  NWNs/FTO electrode

by visual contrast was verified. All the CP curves (Fig. 4a) exhibit deformed triangular shapes, revealing the occurrence of a Faradaic reaction between the  $WO_{3-x}$  NWNs and the  $Al^{3+}$  ions. The corresponding optical performance of the electrode at different current densities was recorded, and the results are shown in Supplementary Fig. S12. It is obvious that the time for the charge/discharge process and the response time for bleaching/coloring process of the electrode are reduced synchronously with the increase of the current density, which is because  $Al^{3+}$  ions cannot participate completely in the redox reaction of  $WO_{3-x}$  NWNs at high current density. In Fig. 4b, the color of the  $WO_{3-x}$  NWNs/FTO electrode gradually turns dark blue when it is discharged to  $-0.6$  V. While in the reverse charging process, the electrode returns to transparent, and the charge storage state can be effectively revealed by a broad range of optical modulations. In other words, the energy storage level of the electrode can be visually monitored by its color. At a current density of 2  $mA\ cm^{-2}$ , the areal specific capacitance of the  $WO_{3-x}$  NWNs obtained from the CP performance is calculated to be 60.02  $mF\ cm^{-2}$ , and the corresponding  $\Delta T$  reaches  $\sim 64.98\%$  (Supplementary Fig. S12). A diagram (Fig. 4c) of

the areal specific capacitance of the  $\text{WO}_{3-x}$  NWNs/FTO electrode determined from the CP curves and the corresponding transmittance change as a function of the current density were drawn according to Supplementary Equation 2 and the results of Supplementary Fig. S12. With increasing current density, the areal specific capacitance and  $\Delta T$  of the  $\text{WO}_{3-x}$  NWNs/FTO electrode gradually decrease and finally reach relatively stable values of  $\sim 15.78 \text{ mF cm}^{-2}$  and 38.48%, respectively.

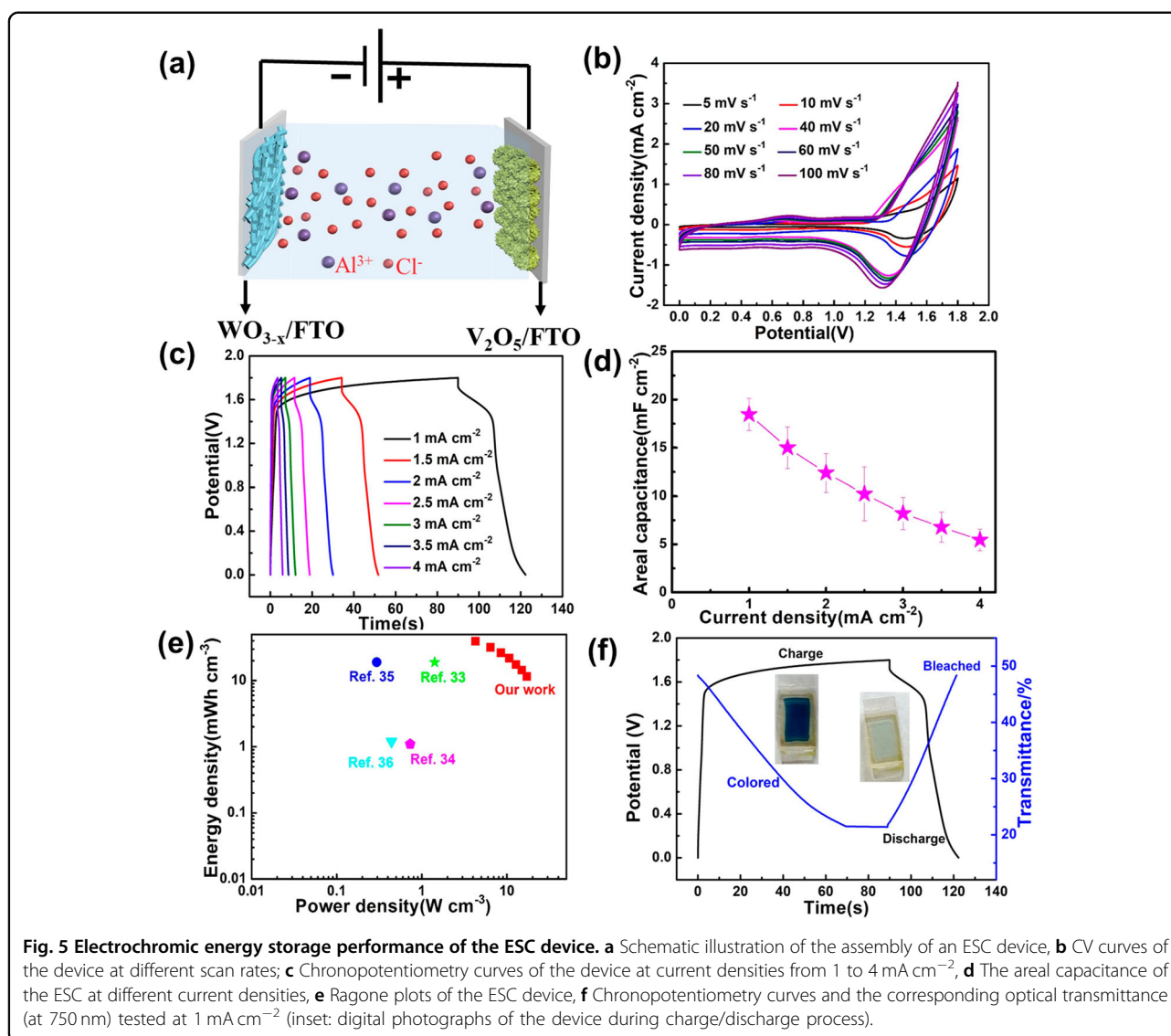
To evaluate the stability of the  $\text{WO}_{3-x}$  NWNs/FTO electrode, cycling tests were examined. As shown in Fig. 4d, the electrode retains 87.53% of its initial specific capacitance and 75.42% of its initial optical modulation (Supplementary Fig. S13a-c) after 10,000 consecutive CV cycles, indicating excellent electrochemical and optical stability. The excellent optical-electrochemical stability of the  $\text{WO}_{3-x}$  NWNs/FTO electrode can lay a foundation for real-world application as an electrode for an ESC device. Electrochemical impedance spectroscopy (EIS) was used to further reveal the cycle performance of the  $\text{WO}_{3-x}$  NWNs/FTO electrode at the open circuit potential. The resultant EIS spectra of the electrode after 1 cycle and after 10,000 cycles are shown in Supplementary Fig. S13d. The values of  $R1$  and  $R2$  after 10,000 cycles increase slightly compared with those after the 1st cycle. This result is in accordance with Fig. 4d, indicating the excellent cycling stability of the  $\text{WO}_{3-x}$  NWNs/FTO electrode. In addition, the increased slope after 10,000 cycles at low frequency shows a low Warburg resistance, indicating high  $\text{Al}^{3+}$  ion diffusion in the structure of the  $\text{WO}_{3-x}$  NWNs/FTO electrode.

Based on the above results, an ESC device was constructed using  $\text{WO}_{3-x}$  NWNs/FTO and  $\text{V}_2\text{O}_5$  nanoflowers/FTO ( $\text{V}_2\text{O}_5$  NFs/FTO) as the cathode and anode, respectively, and  $1 \text{ mol L}^{-1} \text{ AlCl}_3$  as the electrolyte. A schematic illustration of the device is shown in Fig. 5a. Information on the physicochemical and electrochemical properties of  $\text{V}_2\text{O}_5$  NFs/FTO is presented in Supplementary Fig. S14. The relevant evaluation of ESC device construction is also shown in Supplementary Fig. S15. Figure 5b shows the CV curves of the ESC device at different scan rates of  $5\text{--}100 \text{ mV s}^{-1}$ . The CV curves have a nonrectangular shape with broad redox peaks, which indicates a faradaic redox process. Furthermore, in Fig. 5c, the CP curves of the device at various current densities show asymmetrical triangular shapes, which are in accordance with the results of the CV measurement. According to the discharge curves of the ESC device, the calculated specific areal capacitances range from 18.46 to  $5.44 \text{ mF cm}^{-2}$  as the current density increases from 1 to  $4 \text{ mA cm}^{-2}$  based on the total area of the device (Fig. 5d). To evaluate the charge storage characteristics of the ESC device, the energy density ( $E$ ) and corresponding power density ( $P$ ) were computed from Supplementary Equations 4 and 5, and the results are shown in Fig. 5e. The device delivers a high energy density

of  $39.34 \text{ mWh cm}^{-3}$  at a power density of  $4.26 \text{ W cm}^{-3}$ , and can still maintain  $11.61 \text{ mWh cm}^{-3}$  at a power density of  $17.05 \text{ W cm}^{-3}$ , which is comparable to or higher than those of previously reported thin film-based asymmetric supercapacitors (ASCs), including  $\text{WO}_3/\text{V}_2\text{O}_5$  hybrid thin film devices ( $19 \text{ mWh cm}^{-3}/1.42 \text{ W cm}^{-3}$ )<sup>33</sup>,  $\text{WO}_3/\text{WO}_3/\text{MnO}_2$  ASCs ( $1.2 \text{ mWh cm}^{-3}/0.411 \text{ W cm}^{-3}$ )<sup>34</sup>, PANI// $\text{WO}_{3-x}/\text{MoO}_{3-x}$  ASCs ( $1.1 \text{ mWh cm}^{-3}/0.73 \text{ W cm}^{-3}$ )<sup>35</sup>, and SCNT/PANI//SCNT/ $\text{W}_{18}\text{O}_{49}$  ASCs ( $19 \text{ mWh cm}^{-3}/295 \text{ mW cm}^{-3}$ )<sup>36</sup>.

To verify the ability of in situ visual monitoring of the charge storage state of the transparent capacitors, the energy storage state and the corresponding optical state of the device are studied synchronously. Figure 5f shows that the color of the ESC device gradually turns dark blue, and the transmittance decreases during the charging process, while the color of the device reversibly fades during the discharging process. The ESC device delivers an areal specific capacitance of  $12.40 \text{ mF cm}^{-2}$  with a corresponding  $\Delta T$  (at  $750 \text{ nm}$ ) of 26.85% at  $1 \text{ mA cm}^{-2}$ . In addition, the specific capacity and color of the device in the discharge process are also studied in detail in Supplementary Fig. S16. It is found that each energy status of the device is monitored by the corresponding visual color. In the charging process,  $\text{Al}^{3+}$  ions are released from the  $\text{V}_2\text{O}_5$  NFs/FTO electrode and then embedded in the  $\text{WO}_{3-x}$  NWNs/FTO electrode, accompanied by the device color turning dark blue. When the devices are completely discharged, the color of the ESC device changes from dark blue to transparent. The above results evidently prove the possibility of quantitatively monitoring the energy storage level by the optical performance, which is a convenient and effective indicator for the energy level of an energy storage device<sup>37</sup>.

The superior dual-function integrated performance of the ESC might be attributed to the following reasons: (1) The crosslinked nanowire networks of the 3D  $\text{WO}_{3-x}$  NWN/FTO electrode with a hierarchical pore structure can provide a large number of active sites, shorten the ion diffusion paths, enhance redox reactions and alleviate the expansion of  $\text{WO}_{3-x}$  NWNs caused by the  $\text{Al}^{3+}$  ion reaction, resulting in high capacitance and a large corresponding  $\Delta T$ . (2) The direct growth of  $\text{WO}_{3-x}$  NWNs on FTO glass can increase the adhesion force and reduce the extra contact impedance, benefitting the rapid transfer of electrons. (3) The synergistic electrochemical reactions between the  $\text{Al}^{3+}$  ion intercalation behavior and the surface pseudocapacitance reaction contribute to the electrochemical and optical properties of the electrode. (4) The  $\text{V}_2\text{O}_5$  NF/FTO electrode, which matches well with the 3D  $\text{WO}_{3-x}$  NWN/FTO electrode, provides high optical transmittance and good electrochemical performance, beneficial to achieving ESC devices with high optical-electrochemical performance.



## Conclusions

In this work, we successfully prepared a 3D WO<sub>3-x</sub> NWNs/FTO electrode through a solvothermal method combined with a calcination process. Based on the results of an operando spectra-electrochemical synchronous test, the WO<sub>3-x</sub> NWNs/FTO cathode exhibits a high areal specific capacitance (57.57 mF cm<sup>-2</sup>) with a corresponding large  $\Delta T$  (85.05%) and excellent cycling stability (specific capacitance retention of 87.53% and homologous optical modulation range retention of 75.42% after 10,000 cycles) owing to the 3D crosslinked nanowire network structure, hierarchical porous channel, large specific area and strong adhesion with the FTO substrate. In addition, the reaction mechanism was further revealed and verified by in situ XRD, which demonstrated the behavior of surface pseudocapacitance and the inserted reaction that occurred at

different voltage intervals. Furthermore, an ESC device based on the WO<sub>3-x</sub> NWNs/FTO cathode and V<sub>2</sub>O<sub>5</sub> NFs/FTO anode shows high capacity and large optical modulation. Remarkably, the charge storage state of the ESC can be intelligently quantified by the corresponding color of the device during the charging/discharging process, thus realizing the color-to-energy monitoring of the ESC. This study offers new insights for developing integrated intelligent supercapacitors.

## Experimental section

Information regarding the raw materials and solvents used in this experiment, the construction of 3D WO<sub>3-x</sub> NWNs/FTO, V<sub>2</sub>O<sub>5</sub> NFs/FTO, and asymmetric ESC devices, in situ XRD methods, area capacitance, energy density and power density calculations are all offered in the Supporting Information.

### Acknowledgements

We acknowledge support from the National Key Research & Development Program (2016YFB0303903, 2016YFE0201600) and the Foundation of Equipment Development Department (6220914010901).

### Author details

<sup>1</sup>School of Chemistry and Chemical Engineering, Harbin Institute of Technology, 150001 Harbin, PR China. <sup>2</sup>Henan Provincial Key Laboratory of Surface and Interface Science, Department of Materials and Chemical Engineering, Zhengzhou University of Light Industry, 450002 Zhengzhou, PR China. <sup>3</sup>Center for Composite Materials and Structure, Harbin Institute of Technology, 150001 Harbin, PR China

### Competing interests

The authors declare no competing interests.

### Publisher's note

Springer Nature remains neutral with regard to jurisdictional claims in published maps and institutional affiliations.

**Supplementary information** The online version contains supplementary material available at <https://doi.org/10.1038/s41427-021-00319-7>.

Received: 9 March 2021 Revised: 7 May 2021 Accepted: 4 June 2021

Published online: 09 July 2021

### References

- Zhou, S. et al. An electrochromic supercapacitor based on an MOF derived hierarchical-porous NiO film. *Nanoscale* **12**, 8934–8941 (2020).
- Kim, J. et al. Nanofilament array embedded tungsten oxide for highly efficient electrochromic supercapacitor electrodes. *J. Mater. Chem. A* **8**, 13459–13469 (2020).
- Wang, Z. et al. Remarkable near-infrared electrochromism in tungsten oxide driven by interlayer water-induced battery-to-pseudocapacitor transition. *ACS Appl. Mater. Interfaces* **12**, 33917–33925 (2020).
- Shen, W., Huo, X., Zhang, M. & Guo, M. Synthesis of oriented core/shell hexagonal tungsten oxide/amorphous titanium dioxide nanorod arrays and its electrochromic-pseudocapacitive properties. *Appl. Surf. Sci.* **515**, 146034 (2020).
- Zhang, H., Xu, H., Endres, F. & Li, Y. Multi-color poly (3-methylthiophene) films prepared by a novel pre-nucleation electrodeposition grown method for enhancing electrochromic stability. *Electrochim. Acta* **362**, 137103 (2020).
- Reddy, B. N., Kumar, P. N. & Deepa, M. A poly (3, 4-ethylenedioxythiophene)-Au@WO<sub>3</sub>-based electrochromic pseudocapacitor. *Chemphyschem* **16**, 377–389 (2015).
- Koo, B. R., Jo, M. H., Kim, K. H. & Ahn, H. J. Multifunctional electrochromic energy storage devices by chemical cross-linking: impact of a WO<sub>3</sub>·H<sub>2</sub>O nanoparticle-embedded chitosan thin film on amorphous WO<sub>3</sub> films. *NPG Asia Mater.* **12**, 1–12 (2020).
- Liu, L. et al. High-temperature adaptive and robust ultra-thin inorganic all-solid-state smart electrochromic energy storage devices. *Nano Energy* **62**, 46–54 (2019).
- Guo, Q., Zhao, X., Li, Z., Wang, D. & Nie, G. A novel solid-state electrochromic supercapacitor with high energy storage capacity and cycle stability based on poly (5-formylindole)/WO<sub>3</sub> honeycombed porous nanocomposites. *Chem. Eng. J.* **384**, 123370 (2020).
- Zhang, D. et al. A solar-driven flexible electrochromic supercapacitor. *Materials* **13**, 1206 (2020).
- Huo, X. et al. High-performance electrochromic supercapacitors based on the synergetic effect between aqueous Al<sup>3+</sup> and ordered hexagonal tungsten oxide nanorod arrays. *J. Mater. Chem. A* **8**, 9927–9938 (2020).
- Guo, Q. et al. High performance multicolor intelligent supercapacitor and its quantitative monitoring of energy storage level by electrochromic parameters. *ACS Appl. Energy Mater.* **3**, 2727–2736 (2020).
- Yun, T. Y., Li, X., Kim, S. H. & Moon, H. C. Dual-function electrochromic supercapacitors displaying real-time capacity in color. *ACS Appl. Mater. Interfaces* **10**, 43993–43999 (2018).
- Haizeng, L., Guoying, S., Hongzhi, W., Qinghong, Z. & Yaogang, L. Self-seeded growth of nest-like hydrated tungsten trioxide film directly on FTO substrate for highly enhanced electrochromic performance. *J. Mater. Chem. A* **2**, 11305–11310 (2014).
- Zhao, Y. M. et al. Two-dimensional tungsten oxide nanowire networks. *Appl. Phys. Lett.* **89**, 133116 (2006).
- Velmurugan, R., Alagammai, P., Ulaganathan, M. & Subramanian, B. High performance in situ annealed partially pressurized pulsed laser deposited WO<sub>3</sub> & V<sub>2</sub>O<sub>5</sub> thin film electrodes for use as flexible all solid state supercapacitors. *J. Mater. Chem. A* **8**, 24148–24165 (2020).
- Jain, R. K., Khanna, A., Gautam, Y. K. & Singh, B. P. Sputter deposited crystalline V<sub>2</sub>O<sub>5</sub>, WO<sub>3</sub> and WO<sub>3</sub>/V<sub>2</sub>O<sub>5</sub> multi-layers for optical and electrochemical applications. *Appl. Surf. Sci.* **536**, 147804 (2021).
- Nayak, A. K., Das, A. K. & Pradhan, D. High performance solid-state asymmetric supercapacitor using green synthesized graphene-WO<sub>3</sub> nanowires nanocomposite. *ACS Sustain. Chem. Eng.* **5**, 10128–10138 (2017).
- Chen, D., Gao, L., Yasumori, A., Kuroda, K. & Sugahara, Y. Size- and shape-controlled conversion of tungstate-based inorganic-organic hybrid belts to WO<sub>3</sub> nanoplates with high specific surface areas. *Small* **4**, 1813–1822 (2008).
- Danine, A. et al. Room Temperature UV treated WO<sub>3</sub> thin films for electrochromic devices on paper substrate. *Electrochim. Acta* **129**, 113–119 (2014).
- Li, Y. et al. Preparation of oxygen-deficient WO<sub>3-x</sub> nanosheets and their characterization as anode materials for high-performance Li-ion batteries. *Electrochim. Acta* **298**, 640–649 (2019).
- Liu, Z. et al. Low-temperature combustion synthesis of hexagonal WO<sub>3</sub>·0.33H<sub>2</sub>O@C as anode material for lithium ion batteries. *J. Alloy. Compd.* **701**, 215–221 (2017).
- Wu, X. & Yao, S. Flexible electrode materials based on WO<sub>3</sub> nanotube bundles for high performance energy storage devices. *Nano Energy* **42**, 143–150 (2017).
- Kabtam, D. M. et al. Three-dimensional annealed WO<sub>3</sub> nanowire/graphene foam as an electrocatalytic material for all vanadium redox flow batteries. *Sustain. Energy Fuels* **1**, 2091–2100 (2017).
- Li, J. et al. Tunable stable operating potential window for high-voltage aqueous supercapacitors. *Nano Energy* **63**, 103848 (2019).
- Owusu, K. A. et al. Low-crystalline iron oxide hydroxide nanoparticle anode for high-performance supercapacitors. *Nat. Commun.* **8**, 1–11 (2017).
- Yu, F. et al. Pseudocapacitance contribution in boron-doped graphite sheets for anion storage enables high-performance sodium-ion capacitors. *Mater. Horiz.* **5**, 529–535 (2018).
- Wang, S. et al. Transition-metal oxynitride: a facile strategy for improving electrochemical capacitor storage. *Adv. Mater.* **31**, 1806088 (2019).
- Zhao, Z. et al. Designing two-dimensional WS<sub>2</sub> layered cathode for high-performance aluminum-ion batteries: From micro-assemblies to insertion mechanism. *Nano Today* **32**, 100870 (2020).
- Li, Y. et al. Design of TiO<sub>2</sub>@C hierarchical tubular heterostructures for high performance potassium ion batteries. *Nano Energy* **59**, 582–590 (2019).
- Li, H., Firby, C. J. & Elezabi, A. Y. Rechargeable aqueous hybrid Zn<sup>2+</sup>/Al<sup>3+</sup> electrochromic batteries. *Joule* **3**, 2268–2278 (2019).
- Wang, P. et al. A flexible aqueous Al ion rechargeable full battery. *Chem. Eng. J.* **373**, 580–586 (2019).
- Ramasamy, V., Palaniappan, A., Mani, U. & Subramanian, B. High performance of in-situ annealed partial pressurized pulsed laser ablated (PLD) WO<sub>3</sub> & V<sub>2</sub>O<sub>5</sub> thin film electrodes for flexible all solid state supercapacitors. *J. Mater. Chem. A* **8**, 24148–24165 (2020).
- Sarkar, D., Mukherjee, S., Pal, S., Sarma, D. & Shukla, A. Hexagonal WO<sub>3</sub> nanorods as ambipolar electrode material in asymmetric WO<sub>3</sub>/WO<sub>3</sub>/MnO<sub>2</sub> supercapacitor. *J. Electrochem. Soc.* **165**, A2108 (2018).
- Xiao, X. et al. WO<sub>3-x</sub>/MoO<sub>3-x</sub> core/shell nanowires on carbon fabric as an anode for all-solid-state asymmetric supercapacitors. *Adv. Energy Mater.* **2**, 1328–1332 (2012).
- Li, K. et al. Aluminum-ion-intercalation supercapacitors with ultrahigh areal capacitance and highly enhanced cycling stability: power supply for flexible electrochromic devices. *Small* **13**, 1700380 (2017).
- Liu, L. et al. High-performance all-inorganic portable electrochromic Li-ion hybrid supercapacitors toward safe and smart energy storage. *Energy Storage Mater.* **33**, 258–267 (2020).